Title

Characterizing In-Plane Geometrical Variability in Textile Ceramic Composites

Journal

Journal of the American Ceramic Society, 98(1)

ISSN

0002-7820

Authors

Rossol, Michael N

Fast, Tony

Marshall, David B

et al.

Publication Date

2015

DOI

10.1111/jace.13275

Peer reviewed

journal

J. Am. Ceram. Soc., 98 [1] 205–213 (2015)
DOI: 10.1111/jace.13275

Characterizing In-Plane Geometrical Variability in Textile Ceramic Composites

Michael N. Rossol,[‡] Tony Fast,[‡] David B. Marshall,[§] Brian N. Cox,[§] and Frank W. Zok[‡,†]

[‡]Materials Department, University of California, Santa Barbara, California 93106

[§]Teledyne Scientific Company, Thousand Oaks, California 91360

We present a methodology for characterizing and reconstructing in-plane weave variability in textile composites. Surface topography of a partially processed C-fiber/SiC matrix composite panel was measured using digital image correlation. The centroids of tow segments that appear periodically on the fabric surface were located by image analysis and used as fiducial markers. Stochastic deviations of the fiducial markers from the ideal periodic weave structure indicate geometrical variance. Fourier analysis shows that spatial wavelengths of the deviations range from the size of one unit cell to the dimensions of the entire panel. Long-range deviations are attributed principally to fabric deformation after manufacture, during handling. Short-range fluctuations, extracted by computing spatial derivatives of the positions of the fiducial markers, are attributed to variations in tow packing density that arises during weaving. A simple set of statistics for these deviations is presented and its use in generating stochastic virtual specimens is demonstrated.

I. Introduction

Woven textile ceramic composites represent an important class of emerging thermostructural materials, targeted for use in turbine engines, rockets, hypersonic flowpaths, and thermal protection systems. Relative to their laminated counterparts, woven systems provide increased flexibility for fiber placement to best match the anticipated thermal and mechanical stress fields. For instance, tubular structures that must support high internal pressures can be designed with fibers that follow the maximum principal stress directions and in proportions that correspond to the ratio of these stresses (2:1 in cylindrical tubes). In addition, they can be configured to pass through the thickness of thin structures to mitigate delamination failures and to enhance heat flow in high heat flux applications. Indeed, thin woven C/SiC composites have been demonstrated to sustain temperature gradients exceeding 1000 K/mm without failure.[1] They also allow for integral forming of holes or slots (for cooling, for example) without cutting fibers as well as integral attachment to other structural elements.[1] But with increasing weave complexity comes the possibility of increasing defects in tow trajectories and shapes. The nature of these defects and their effects on thermomechanical performance represent key issues that must be addressed in order for these composites to be successfully implemented in critical components.

Synchrotron X-ray computed tomography (CT) has been shown to provide exquisite detail in the geometric characteristics and defects with ca. μm resolution in woven ceramic composites.[2-4] It has been used to establish statistical descriptors of the shapes and positions of tows.[2] In turn, these descriptors have been used in conjunction with a probabilistic geometry generator to create virtual specimens with the same statistical characteristics as those obtained from the CT images.[4] In this way, the effects of defect distributions on thermal and mechanical performance can be probed computationally.[3] Despite the richness of information extracted from CT images, the technique has one major drawback: that of severely restricted volume and shape of specimens that can be characterized. While extensive work has been done in the textile community to enable automated detection of defects in large woven material, the techniques are fundamentally qualitative, with defects only needing to be identified and located, not quantified and characterized.[5–8]

The objective of the this article was to present a methodology for characterizing long-range weave defects using a complementary characterization technique, based on surface topography mapping via 3D digital image correlation (DIC). Although DIC mapping is inherently limited to characterization of external surfaces, the surfaces of woven composites of interest (described below) constitute a significant fraction of all tow surfaces. Consequently, the technique is expected to provide substantial information (although clearly not comprehensive) on geometric tow defects that cannot be gleaned from CT imaging alone.

In addition to procedures for acquiring and stitching multiple DIC data sets, analytical methods are presented for characterizing deviations of the weave from a hypothetical perfectly-periodic structure using the positions of one population of surface tows as fiducial markers. The methods include partitioning of the deviations into short- and long-range components, calculation of their spatial derivatives (to enhance the visibility of the short-range components) and spectral analysis of the derivatives using Discrete Fourier Transforms. Panel curvatures also emerge from these analyses. The methods are demonstrated on a composite panel that appears quite regular to the unaided eye. Their application to characterization of panels with intentionally-introduced defects and the role of such defects on composite properties will be presented in forthcoming publications.

While demonstrated here for a representative 3D woven ceramic matrix composite, the methods are applicable to any woven or braided product with nominally periodic architecture. The shorter range variations in tow packing density reported below are concluded to be generated by the weaving machinery and therefore might be endemic to weaves. Indeed, qualitative characteristics are very similar to those reported elsewhere for 2D twill weaves of carbon fibers intended for use with polymer matrices.[9]

R. S. Hay—contributing editor

Manuscript No. 35007. Received May 15, 2014; approved September 4, 2014.
[†]Author to whom correspondence should be addressed. e-mail: zok@engineering.ucsb.edu

II. Experimental Methods

(1) Material

The material of interest for this study was a woven C-SiC composite comprising a three-layer angle interlock weave of T300-6K carbon fibers. The architecture is shown in Fig. 1. The composite was infiltrated first with pyrolytic carbon to provide a weak debond layer around the individual fibers, then with CVI SiC, to form a 40μm-thick matrix layer, which sealed the fiber tows, and rigidified the preform. The composite was examined in this partially processed state; upon full densification many of the surface features of interest are obscured. The panel had dimensions 157 mm × 116 mm in the weft and warp directions, respectively, and an average thickness of 1.36 mm. It had been cut from a larger panel that was about 170 mm wide (weft direction) and about 320 mm long (warp direction).

(2) Measurement Details

In preparation for DIC imaging, high-contrast speckle patterns were created on both panel faces by spraying the surfaces with white water-soluble paint using an airbrush. (The usual technique of first painting the surface with a solid color before speckling proved unnecessary because the panel surface was almost black[10]). Speckles produced using this technique have an average size of approximately 100 μm.[11]

Images were acquired using two digital cameras (Point Grey Research Grasshopper, Richmond, BC, Canada), each with a CCD resolution of 2448 × 2048 pixels and a 70–180 mm lens (Nikon ED AF Micro Nikkor, Nikon Inc., Melville, NY). The focal length of the lenses was 70 mm, the aperture setting was F-16, and the magnification was 23 μm/pixel. The angle between the cameras was 27°. To retain high resolution, images were taken of subsections of the surface (47 mm × 56 mm in size) and subsequently stitched together using methods described below. To facilitate stitching, an overlapping region about 10 mm wide was included in adjacent images. With the present selection of imaging parameters and the panel dimensions, 12 image pairs were required to characterize each of the two panel faces.

Correlation of the images was carried out using Vic-3D software (Correlated Solutions, Columbia, SC). The images were correlated with a subset size of 21 pixels and a step size of two pixels.[12] These settings have previously been shown to yield satisfactory results in characterizing the surface topography of this composite.[12] The raw topographic data, represented by the function $z(x,y)$ relating surface height z to in-plane coordinates x and y, were exported from Vic-3D, with subsequent data stitching and further analysis performed using Mathematica® (Wolfram Research, Champaign, IL).

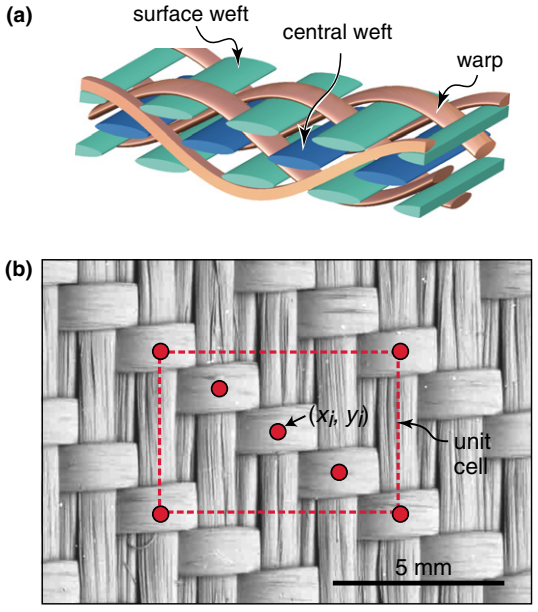

Fig. 1. Unit cell of three-layer angle interlock weave of present interest: (a) schematic showing the three genuses of tows and (b) optical image of the composite in plan view. Also shown in (b) is a set of grid points used for least-squares fitting of the deviations (u_j, v_j) at point (x_i, y_i), as described in Section V.

III. Extracting Tow Information from Surface Topography

(1) Stitching Data Sets

Stitching of two adjacent data sets requires that both be in the same reference frame. This goal was accomplished by first identifying three distinct speckles (to serve as fiducial markers) in the overlapping field and then repositioning one of the images in-plane such that speckles were brought into alignment. The requisite positional shifts and rotation were determined by minimizing the sum of the squares of the Euclidean distance between each pair of points in the two images. Following repositioning in-plane, the images were shifted in the z-direction so that the mean surface heights in the two images were the same. For the purpose of the segmentation operations described below, the data for each panel face were auto-plane fit, to move them from the plane of the camera CCD to the x–y plane. The full topographic map for one panel face constructed in this manner is shown in Fig. 2.

(2) Segmentation of Data

The present weave consists of four distinct genuses of fiber tows,[4] three of which appear on the specimen surface: surface wefts, center wefts, and warp tows [Fig. 1(a)]. The portions of tows that are visible on the surface exhibit characteristic variations of height and outline in the x–y plane. Although the height ranges for different tow genuses overlap, automated attribution of each visible tow segment to a particular genus was possible by combining height and shape information. The data were segmented into subsets for each tow genus using the following procedures.

First, common features were brought to comparable heights over the entire panel area by subtracting from each $z(x,y)$ value the mean *local* surface height $\bar{z}_{local}(x,y)$, computed over an area of one unit cell centered on (x,y). The warp tows and the surface wefts, which generally stand higher than the central wefts on the surface, were separated

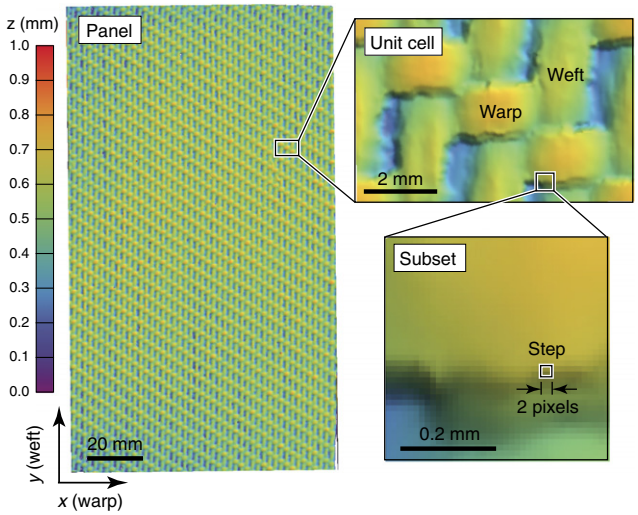

Fig. 2. Surface topography at various length scales of one face of the composite panel. Slight gradient in height from panel edges inward in (a) is a manifestation of panel curvature.

from the latter by thresholding the distribution of the quantity $z(x,y) - \bar{z}_{local}(x,y)$ [Fig. 3(a)]. The warp tows and surface wefts were then classified using information about the aspect ratios of the outlines formed by the thresholding procedure: the average aspect ratio of the warp crowns is slightly greater than unity, whereas that of the surface wefts is less than 0.5. The distributions in aspect ratios are plotted in Fig. 3(b) and the segmented warp and surface weft tows are shown in Fig. 3(c).

The outlines formed by thresholding are more consistent for warp tows, which appear on the surface as relatively regular crown features than they are for weft tows. Therefore, the segmented domains formed by thresholding data for warp tows were used exclusively for analyzing weave characteristics.

An ancillary result of computing local heights averaged over a unit-cell gauge length is the spatial distribution in averaged surface heights $\bar{z}_{\text{local}}(x,y)$; fitting the data yields the two principal curvatures of the panel and their directions. The results for the two panel faces, plotted in Fig. 4, show that the principal curvatures are aligned approximately with the fiber directions. In addition, the slight differences in the surface heights on the two faces indicate slight nonuniformity in the panel thickness. Examinations of corresponding line scans on the two faces (not shown) indicate that these variations are not greater than about 40 μm.

(3) Definition and Interpretation of Warp Crown Positions

Analysis begins by computing the position (x_i,y_i) of the centroid of the segment area for each of N visible warp crowns, with $i = 1, \ldots, N$.[¶] This position represents the midpoint of the intersection of the projections on the x–y plane of the warp tow visible on the surface and the underlying weft tow. With the y-axis assigned to the weft direction, variations in the component y_i describe lateral shifts in the position of the warp tow, while variations in the component x_i describe lateral shifts in the position of the underlying weft tow (Fig. 5). Any shifts of either the warp or weft tows along their own axes remain undetermined.

Since the fabricated product was intended to be and is often modeled as being regular and periodic, it is useful to extract from the stochastic data an ideal perfectly-periodic structure and regard the measured textile as being a deviation from this perfect structure. The ideal structure is one that would be used in nonstochastic modeling of the composite to predict mean composite properties. The degree to which the real material departs from the ideal should correlate with the measured scatter in properties if that scatter is due to variations in the weave structure.

The determination of the unit cell size and orientation for the hypothetical ideal is described below. Each warp crown position (x_i,y_i) can be regarded as shifted by a deviation vector (u_i,v_i) from the location $(\bar{x}_i, \bar{y}_i)$ that the warp crown would have in the hypothetical ideal:

$$(x_i, y_i) = (\bar{x}_i, \bar{y}_i) + (u_i, v_i). \tag{1}$$

All analysis is conducted using the array of positions (x_i, y_i) or deviations (u_i,v_i), which are defined over a periodic grid, $(\bar{x}_i, \bar{y}_i)$, with four grid points (four warp crowns) per unit cell of the fabric (the unit cell is defined as the smallest orthorhombic repeat unit of the ideal weave structure, Figs. 1 and 3).

[¶]An alternative choice of position to represent a warp crown segment is that at which the surface height is maximum within the segment. The maximal positions were calculated by fitting the data to a second-order polynomial. The resulting positions were almost indistinguishable from those obtained from the tow centroids. For computational expediency, the centroid method is preferred.

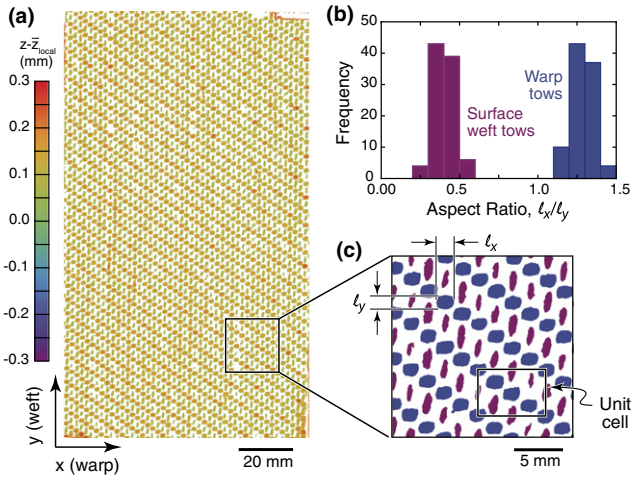

Fig. 3. Results of segmentation process used to isolate tow segments. (a) Thresholding based on local surface heights, (b) subsequent differentiation between wefts and warps based on tow aspect ratios, and (c) resulting surface weft and warp tow segments (shown in purple and blue, respectively).

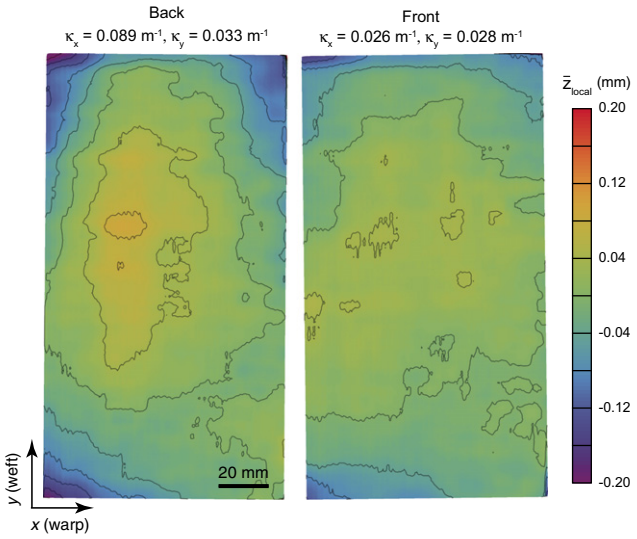

Fig. 4. Distribution in surface heights averaged locally over one unit cell. The distributions were fit to second-order polynomials in both x and y and the fitted function then used to compute the curvatures κ_x and κ_y in the x and y directions, respectively.

(4) Potential Sources of Deviations

The deviations (u_i,v_i) may have arisen during handling of woven fabric (after manufacturing). Alternatively they may have been built into the fabric during the textile manufacturing process. Analysis will suggest that the deviations, in fact, include contributions of both types: namely, long-wavelength contributions caused by fabric deformation and short-wavelength contributions created during the weaving process.

Deviations in the lateral positions of weft tows can arise during "beating up", wherein weft tows that have been newly inserted between warp tows are pushed along the warp tows into the fabric that has already been formed. The position at which the weft stops sliding along the warp tows during beating up is expected to be variable [(Fig. 5(b)]. Deviations in the lateral positions of warp tows might arise during weaving due to interplay between looseness in the heddles that guide the warp tows, variations in the frictional drag imposed by weft tows during their insertion, and nonuniformity in the tensions applied to the warp tows. Variations in the lateral positions of either tow type imply variations in

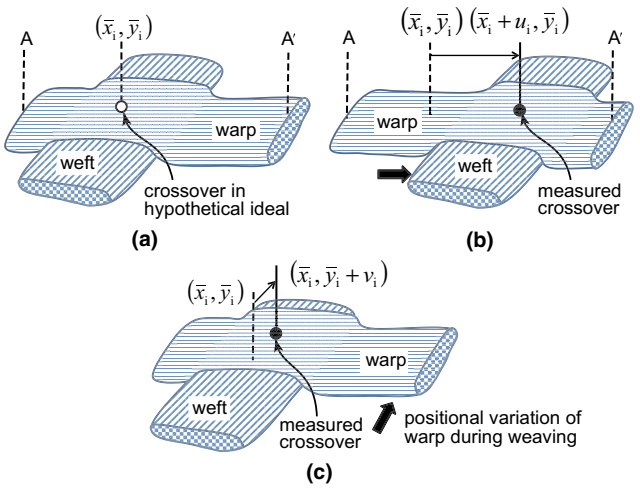

Fig. 5. (a) and (b): A shift of the centroid of a warp crown in the warp direction indicates a lateral variation in the location of the underlying weft. (a) and (c): A shift of the centroid of a warp crown in the weft direction indicates a lateral variation in the location of the warp.

the local packing density of tows, which imply variations in the local fiber volume fraction.

Displacements due to deformation of the fabric after its manufacture are usually associated with global shear deformation, which tends to occur by sliding rotations of tows at crossovers. If the global shear is small, it causes minimal change to the local tow packing density. The tow spacing varies as shear strain γ^2; for $\gamma \sim 10^{-2}$, for example, the fractional change in tow spacing is $\sim 10^{-4}$. However, if the shear strain is large (say ~0.1), changes in tow spacing can be so severe that fabric "lock-up" occurs. When shear causes changes in tow spacing, the changes will be uniform over spatial gauge lengths for which the shear strain is uniform.

IV. General Weave Characteristics

Figures 2 and 3 confirm that the weave is an approximately periodic structure. Other broad characteristics of the fabric can be seen by collating the projections of the trajectories of all warp and weft tows onto the x–y plane, shifted in space to bring all of the warp and all of the weft tows separately into coincidence at one end (Fig. 6). The results show that: (1) the projected trajectory of each tow is not straight over length scales larger than the unit-cell dimensions but instead follows a curved path; (2) the projected trajectories of warp tows appear similar to one another when viewed at the macroscopic scale [Fig. 6(a)]; and (3) the projected trajectories of weft tows also appear similar to one another [Fig. 6(b)]. The implication is that each tow population has undergone long-range cooperative deviation from its intended path. In addition to the long-range trends, scatter among the projections indicates short-range positional fluctuations.

The average unit cell in the actual weave structure is defined by the two vectors r_1 and r_2 along the warp and weft directions. These vectors are obtained by determining the average vector connecting neighboring crowns on all warp and weft tows. The mean and standard deviations of their magnitudes over the entire panel area are $r_1 = \lambda_{warp} = 7.52 \pm 0.06$ mm and $r_2 = \lambda_{weft} = 5.05 \pm 0.05$ mm. The average angle between warp and weft tows, obtained from the lattice vectors, is $\theta_{av} = 89.65° \pm 0.06°$.

The direction of r_2 (parallel to the weft tows) was taken to be the y-axis of the specimen; the x-axis was set to be orthogonal to the y-axis. These directions and the lattice dimensions λ_{warp} and λ_{weft} define the ideal weave structure

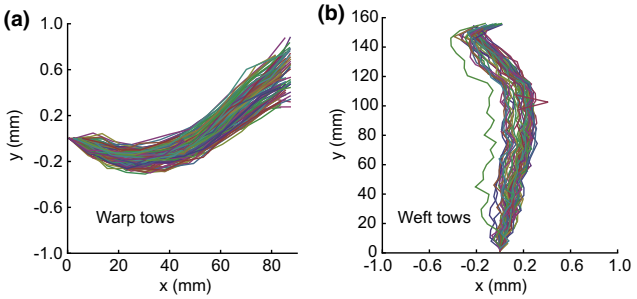

Fig. 6. (a) Warp and (b) weft tow trajectories throughout entire panel. The warp trajectories had been shifted in the y-direction so as to align the left end of each tow with $y = 0$. Similarly, the weft tows had been shifted in the x-direction so as to align the bottom end of each weft with $x = 0$.

to which the deviations of Eqn. (1) refer. The axes in Fig. 7 and other data plots are these axes of the hypothetical ideal.

V. Long- and Short-Range Deviations

Plots of the deviation data, rendered as quasi-continuous quantities by interpolating the arrays (u_i,v_i), show that the largest amplitude deviations are associated with variations that span the entire specimen (Fig. 7). Lower amplitude variations (mild color changes between the discrete contour lines in Fig. 7) occur over shorter spatial gauges.

The visibility of short-wavelength variations relative to those with longer wavelengths can be enhanced by spatial differentiation, which serves as a filter. Spatial derivatives of the deviations were computed at each grid point $(\bar{x}_i, \bar{y}_i)$ from the slopes of planar functions $u_i(x,y)$ and $v_i(x,y)$ fitted using the least-squares method to the deviations (u_j,v_j) at a set of grid points within an area bounded by a unit cell of the weave structure centered on $(\bar{x}_i, \bar{y}_i)$ [Fig. 1(b)]. The spatial derivatives of most interest are: (1) $\delta_{xx} = \partial u/\partial x$, which gives a direct measure of fluctuations in the packing density of weft fiber tows,[††] (2) $\delta_{yy} = \partial v/\partial y$, which gives a direct measure of fluctuations in the packing density of warp fiber tows, and (3) $\delta_{xy} = (\partial u/\partial y + \partial v/\partial x)/2$, which is equal to one-half of the cotangent of the angle, θ, between the warp and weft tows. In the event that the deviations were caused by mechanical deformation of the preform after completion of weaving, the derivatives δ_{xx}, δ_{yy}, and δ_{xy} can be regarded as tensorial strains ε_{xx}, ε_{yy}, and ε_{xy} in a quasi-continuous material, which are meaningful over gauge lengths somewhat larger than the tow spacing. Otherwise, if produced by the weaving process, δ_{xx}, δ_{yy}, and δ_{xy} represent the variances intrinsic to the weaving operation. Maps of these derivatives, rendered as continuous functions by interpolating the arrays of values at the grid points $(\bar{x}_i, \bar{y}_i)$, are shown in Fig. 8.

The map of δ_{xy} in Fig. 8(c) shows long-range variation in the angle between the warp and weft tows along the x-direction, but minimal variation along the y-direction. As discussed above, this systematic variation is attributable to shear deformation during handling after weaving. The magnitude of the shear strain increases approximately linearly with the distance x with a gradient of 0.00022 mm^{-1}. The average shear strain over the area analyzed is 0.003, corresponding to an angle $\theta = 89.65°$ between the warp and weft tows.

Superimposed on the long-range variations in δ_{xy} in Fig. 8(c) are short-range fluctuations over length scales on the order of several unit cell lengths, presumably introduced during the weaving operation. The magnitude of these fluctuations

[††] $\delta_{xx} = \rho^{o}_{weft}/\rho_{weft} - 1$, where ρ_{weft} is the packing density of the weft tows and ρ^{o}_{weft} is the average packing density of the weft tows. Similarly, $\delta_{yy} = \rho^{o}_{warp}/\rho_{warp} - 1$.

(~0.005) is about ¼ of the long-range variation across the field (approximately 0.02).

The map of δ_{xx} in Fig. 8(a) shows a similar long-range gradient (0.00026 mm^{-1}) in the x-direction (along the warp tows). This variation could also be caused by inadvertent fabric deformation after weaving. Because of the waviness of the warp tows, deformation parallel to the fibers would be relatively easy. Here, again, short-range fluctuations in δ_{xx} are superimposed on the long-range variations. In contrast, the map of δ_{yy} in Fig. 8(b) shows only short-range fluctuations. This is consistent with the expectation that, with the weft tows being essentially straight, deformation parallel to the wefts would be difficult.

For further analysis, the long-range deviations (those with wavelength larger than the specimen width) were subtracted from the deviation data in Fig. 7, then the spatial derivatives of the remaining short-range deviations were calculated. The resultant maps are shown in Fig. 9. (The long-range deviations were determined by fitting biquadratic functions to the deviations.) In this form, the derivatives δ^s_{xx} and δ^s_{yy} represent variations in the relative short-range packing densities of the warp and weft tows, which are likely inherent to the weaving process.

The maps in Fig. 9 exhibit highly anisotropic spatial variations, that is, with very different dependences on x and y. The anisotropy arises because the continuity of fibers tends to dampen positional deviations along the tow direction but not transverse to it. Variations in $\delta^s_{yy}(x,y)$ tend to be smaller in the x-direction than in the y-direction. Conversely, variations in $\delta^s_{xx}(x,y)$ tend to be larger in the x-direction than in the y-direction. Thus, variations in $\delta^s_{yy}(x,y)$ and $\delta^s_{xx}(x,y)$ normal to their respective tow direction can be meaningfully subjected to spectral analysis, whereas those along the tow direction cannot (at least in specimens of the current size). An analysis that recognizes the anisotropy in the richness of data follows.

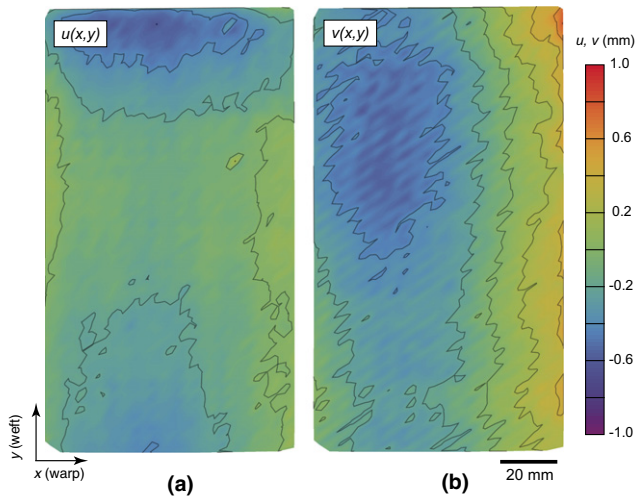

Fig. 7. Quasi-continuous plots of the displacement components, formed by linear interpolation of the discrete data (u_i,v_i), where u and v are displacements in the warp (x) and weft (y) directions, respectively.

VI. Fourier Analysis of Variations in Tow Packing Density

The short-range fluctuations in δ^s_{xx} and δ^s_{yy} were quantified by Fourier analysis. First, each set of data was interpolated to create a data set on a regular grid with spacing $\lambda_{warp}/4$ along all of the warp tows and $\lambda_{weft}/4$ along the weft tows. Discrete Fourier Transforms (DFTs) were then evaluated for $\delta^s_{xx}(x)$ (fluctuations of weft packing density) along successive lines above each warp tow (120 lines, each containing 44 data points) and for $\delta^s_{yy}(y)$ (fluctuations of warp packing density) along lines above the weft tows (44 lines, each containing 120 data points). This yielded a set of Fourier coefficients for each warp line of amplitude $A^{(x)}_m(s)$ and phase $\phi^{(x)}_m(s)$, and for each weft line of amplitude $A^{(y)}_m(s)$ and phase $\phi^{(y)}_m(s)$, where the index m refers to one scan line in the data array and s is the spatial frequency [$s = 1,\ldots(n+1)$], with n the number of data points along the line. The spatial frequencies are defined by a wave number k and a wavelength λ:

$$k(s) = \frac{2\pi}{\lambda(s)} = \frac{2\pi}{L}(s-1) \tag{2}$$

where L is the length of the line.

Comparison of the phases and amplitudes of the Fourier components for all of the warp tows and all of the weft tows indicated substantial stochastic variability. The results are

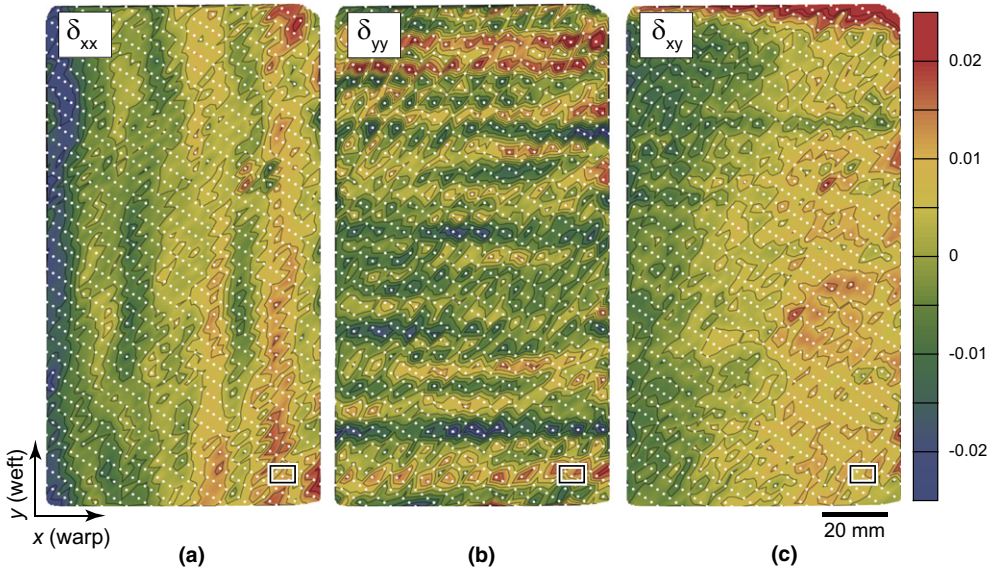

Fig. 8. Quasi-continuous plots of spatial derivatives of the deviation data (u_i,v_i) in Fig. 7 with overlay of warp crown positions. The rectangle in the bottom right corner of each figure represents one unit cell. (The short-range variations are not evident in Fig. 7 because of the coarseness of the displacement scale needed to show the long-range variations).

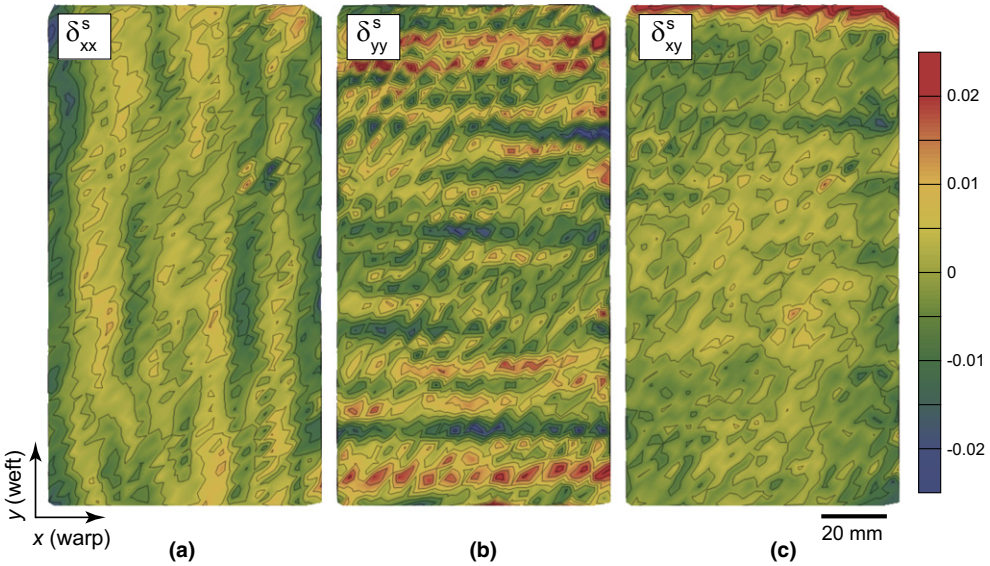

Fig. 9. Quasi-continuous plots of short-range spatial derivatives of the deviation data $(u_i,v_i)_s$.

summarized in Fig. 10, as mean values and standard deviations for each spectral component. Components with significant amplitude are present with wavelengths ranging from the unit cell size ($s = n/4 + 1$ and $n-n/4$) to the specimen width ($s = 2$ and $n-1$). On cursory examination the variation of the amplitude of the Fourier components with s appears qualitatively similar for $\delta^s_{xx}(x)$ and $\delta^s_{yy}(y)$. The distributions of phase angles show very large variances. While only half of the spectral components plotted in Fig. 10 are unique (due to symmetry of the Fourier coefficients about $s = 1 + n/2$), all are needed during the reconstruction of virtual specimens discussed below.

VII. Generation of Stochastic Virtual Specimens

The preceding spectral analysis for characterizing the tow density variations, $\delta^s_{xx}(x)$ and $\delta^S_{yy}(y)$, can be used as a basis for developing simple algorithms for generating ensembles of stochastic virtual specimens. The procedure involves: (1) characterizing the stochastic variations of the amplitudes and phases of the Fourier components in Fig. 10; (2) using a Monte Carlo method to generate other instantiations of the set of Fourier components from the same statistical distribution; and (3) reconstructing the virtual specimen by inverse DFT. Details of the procedure are given in the Appendix.

Figure 11 illustrates an example of the tow density variations generated by the reconstruction algorithm for one virtual specimen, that is, for one choice of pseudo-random numbers. The spatial variations are qualitatively very similar to those seen in the experimental data (Fig. 9). Complete validation of the quality of the reconstruction algorithm requires comparison of data from a large ensemble of virtual specimens with data from a large ensemble of real specimens.

VIII. Discussion

By sampling specimens much larger than the unit cell size, the DIC method has revealed statistical information that could not be discerned in a previous study in which the same composite had been characterized by microcomputed tomography (μCT) of small test specimens (volumes comparable to a single unit cell).[2] In particular, the in-plane deviations in the μCT data were found not to be correlated between different tows,[2] whereas the DIC data reveal that they are indeed correlated over wavelengths larger than the unit cell. These deductions are not contradictory in that longer wavelength correlations between different tows would not be expected to

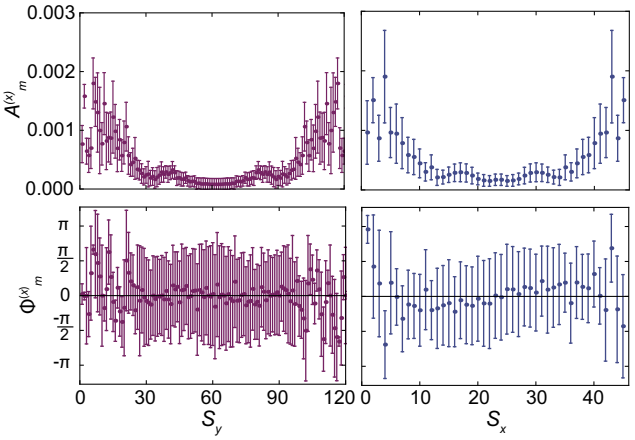

Fig. 10. Distribution of amplitudes and phase from DFTs of all available scans.

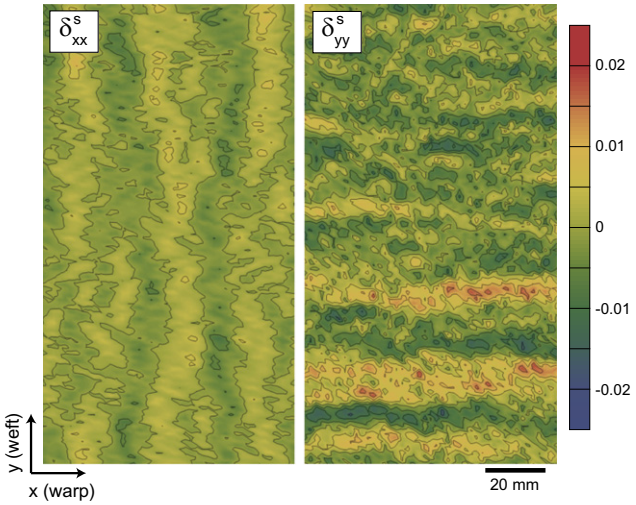

Fig. 11. Packing density variations generated using the reconstruction algorithm.

emerge from data samples of a single unit cell. In such small volumes, the deviations discerned in Fig. 7 would be approximately the same for all tows and would therefore not be

detected as deviations; instead, they would imply a shift in the spatial origin. Thus, the μCT and DIC analyses are complementary: the μCT analysis yielding details of deviations of tow loci and shapes at scales equal to or less than the unit cell size and the DIC analysis yielding deviations with wavelength exceeding the unit cell size. A reasonable assumption is that the statistical trends at different gauge lengths found by the μCT and DIC analyses are statistically independent of each other. In generating virtual specimens, the deviations required to represent short- and long-wavelength variations in the textile would be generated separately and combined by superposition.

Along with the averaged surface height reported in Fig. 4, the displacement, spatial derivatives, and short-range deviations were also calculated for the back side of the panel and can be found in Fig. S1. The pattern of short-range deviations on the front and the back of the panel was found to be very similar. This suggests a high degree of correlation in the motion of tows on both sides of the panel during the weaving process. In addition, the high degree of correlation between the front and back faces of the panel, which were created from independent sets of DIC images, suggests that error in the DIC measurements and stitching procedures are small in comparison with the intrinsic deviations in the weave. While the error has not been directly quantified through replicate analysis of the panel, this conclusion is further supported by more recent work on different panels of the same weave, characterized using analogous procedures, which show the same intrinsic variations in tow packing densities.

The magnitudes and qualitative characteristics of the tow positional variations (or packing density variations) determined for the 3D woven carbon/SiC composite studied here are remarkably similar to those determined in a contemporary study of a carbon fiber 2D twill weave intended for consolidation with a polymer matrix.[9] Long-range deviations found for the twill weave are similar, exhibiting a wavelength comparable to the specimen dimension, again suggesting shear deformation resulting from handling of the manufactured fabric. Short-range deviations are also similar, comprising multiple wavelengths between the unit cell size and the specimen size, and exhibiting similar anisotropy in the variation of deviations in directions parallel and normal to the tow direction. The similarity of short-range deviations suggests that the observed variance results from variance in loom actions that may be characteristic of weaving machinery, that is, qualitatively consistent for different looms.

Variations of the magnitude determined in this work are expected to have minimal effect on the ultimate tensile strength and failure strain of C–SiC composites fabricated from preforms of this type. However, small variations in tow packing density might be expected to affect infiltration and densification of the matrix material within the inter-tow spaces. The resulting variations in the matrix density and pore distribution may bias the locations and loads for crack initiation and hence compromise the resistance of the composite to environmental attack.

In any case, the results of this study have shown that the sensitivity of the measurement and analysis methods presented here is more than sufficient to characterize more severe weave defects that would have a larger impact on composite properties. Therefore, the test methodologies could be readily adopted as part of quality assurance protocols that could be carried out at various stages of composite fabrication.

IX. Conclusions

A methodology for determining in-plane weave characteristics and departures from an ideal periodic weave structure in textile ceramic composites has been developed. The methodology involves:

1. Determination of surface topography using high-resolution image pairs and 3D image correlation;
2. Identification and segmentation of the positions of a prescribed population of surface tows for use as fiducial markers;
3. Determination of a hypothetical perfectly periodic pattern that best fits the stochastic positional data for tows;
4. Determination of in-plane deviations in the nodal positions from their positions in the hypothetical ideal and partitioning of these deviations into short- and long-range components;
5. Determination of spatial derivatives of deviations; and
6. Spectral analysis of the spatial derivatives in the direction transverse to either set of tows by DFT, combined with simple models of the rate at which the complex amplitude of each Fourier component varies in the direction parallel to that set of tows.

The statistical representation of a composite consists of the following set of parameters:

$$S = S_{\text{per}} \cup S_{\text{weft}} \cup S_{\text{warp}} \tag{3a}$$

$$S_{\text{per}} = \lambda_{\text{warp}}, \lambda_{\text{weft}} \tag{3b}$$

$$S_{\text{weft}} = \left\{ M_{\text{A}}^{(\text{y})}(s), \sigma_{\text{A}}^{(\text{y})}(s), \kappa_{\text{A}}^{(\text{y})}(s), \kappa_{\phi}^{(\text{y})}(s), s = 1, \ldots \right\} \tag{3c}$$

$$S_{\text{warp}} = \left\{ M_{\text{A}}^{(\text{x})}(s), \sigma_{\text{A}}^{(\text{x})}(s), \kappa_{\text{A}}^{(\text{x})}(s), \kappa_{\phi}^{(\text{x})}(s), s = 1, \ldots \right\} \tag{3d}$$

where λ_{warp} and λ_{weft} are the lattice parameters of the fitted hypothetical perfectly periodic structure; $M_{\text{A}}^{(\text{y})}(s)$ and $\sigma_{\text{A}}^{(\text{y})}(s)$ are the mean and standard deviation of the amplitude of Fourier component s for weft tow density variations transverse to the weft direction; $\kappa_{\text{A}}^{(\text{y})}(s)$ and $\kappa_{\phi}^{(\text{y})}(s)$ are the correlation lengths for variations in the amplitude and phase, respectively, of component s parallel to the weft tow direction; and $M_{\text{A}}^{(\text{x})}(s)$, $\sigma_{\text{A}}^{(\text{x})}(s)$, $\kappa_{\text{A}}^{(\text{x})}(s)$, and $\kappa_{\phi}^{(\text{x})}(s)$ are analogous quantities for warp tows. Values for this data set appear in Table S1.

The algorithm for constructing virtual specimens consists essentially of reversing the steps outlined above. Values for the amplitude and phase of each Fourier coefficient are determined using a Monte Carlo method. The amplitude is evaluated for a sequence of scan lines using the Markov Chain algorithm, calibrated by $M_{\text{A}}^{(\text{x})}(s)$, $\sigma_{\text{A}}^{(\text{x})}(s)$, $\kappa_{\text{A}}^{(\text{x})}(s)$ for warp tows and $M_{\text{A}}^{(\text{y})}(s)$, $\sigma_{\text{A}}^{(\text{y})}(s)$, $\kappa_{\text{A}}^{(\text{y})}(s)$ for weft tows. Values for the corresponding phase angles are determined by a random walk algorithm calibrated by $\kappa_{\phi}^{(\text{x})}(s)$ for warp tows and $\kappa_{\phi}^{(\text{y})}(s)$ for weft tows. With a complete set of complex Fourier coefficients thus established, the tow packing density variations are determined by inverse DFT and the tow positional deviations are determined from these by integration.

Appendix
Statistical Analysis and Reconstruction Algorithm

1 Statistical Parameter Set for DFT Analysis

The stochastic variations in the amplitudes of the Fourier coefficients for mode s, associated with DFT analysis of weft tow density variations, $\delta_{\text{xx}}^{s}(x, y)$, transverse to the weft direction, are characterized by the mean and standard deviation $M_{A}^{(y)}(s)$ and $\sigma_{A}^{(y)}(s)$ of the amplitude $A_{m}^{(y)}(s)$ and a correlation length κ_{A} derived from Pearson's correlation parameter $C_{A}(k)$ for amplitude values at pairs of scan lines separated by k:

$$\kappa_{A}^{(y)}(s) = \underset{k\,\text{small}}{\text{Mean}} \left(\frac{1 - C_{\text{A}}^{(\text{y})}(k)}{k d_{\text{y}}} \right)^{-1} \tag{A1}$$

where d_y is the scan line spacing, weighted to sample the first few values of k only; and

$$C_A^{(y)}(k) = \frac{\sum_{m,m'} \left(A_m^{(y)}(s) - M_A^{(y)}(s)\right)\left(A_{m'}^{(y)}(s) - M_A^{(y)}(s)\right) \Big/ n_{mm'}}{\hat{\sigma}_A^{(y)}(s)\hat{\sigma}_A'^{(y)}(s)} \quad \text{(A2)}$$

where the sum is over all $n_{mm'}$ pairs of scan lines m and m' for which m–$m' = k$ and the variances $\hat{\sigma}$ and $\hat{\sigma}'$ appearing in the denominator are formed using only those values of $A_m^{(y)}(s)$ or $A_{m'}^{(y)}(s)$ that appear in the numerator when forming the sum.

2 Random Walk Analysis of Phase Angles

Variations in the phase angle for mode s, again associated with DFT analysis of weft tow density variations transverse to the weft direction, are represented by a characteristic length λ_ϕ derived from a random walk analysis. The random walk is defined by:

$$\text{Prob}\{\phi_m - \phi_{m-1} = \delta\phi\} = 0.5$$

$$\text{Prob}\{\phi_m - \phi_{m-1} = -\delta\phi\} = 0.5 \quad \text{(A3)}$$

where ϕ_m is the value taken by the phase variable ϕ on the m^{th} of a sequence of scan lines. The values of ϕ are not confined to a single branch, for example, [0, 2π], but, since a Fourier transform comprises sums of trigonometric functions, the value of a transform is unchanged by $\phi \rightarrow \phi + 2\pi$. Furthermore, if the values generated by the random walk are mapped onto [0, 2π] by adding or subtracting multiples of 2π, the values will be uniformly distributed over [0, 2π] for large enough walks.

For a given grid, the parameter available for calibration is the step size, δφ, which is determined from the set of phase angles $\left\{\phi_m^{(y)}(s), m = 1, \ldots, n_y\right\}$. These data are first conditioned to remove any discontinuities introduced by their having been restricted to the interval [0, 2π] by the algorithm used to compute the DFT:

$$\phi_m^{(y)}(s) \rightarrow \phi_m^{(y)}(s) + \Delta_m \quad \text{(A4)}$$

where

$$\Delta_j = \begin{cases} \Delta_{j-1} + 2\pi & \text{if} \phi_s^{(j)} - \phi_s^{(j-1)} < \pi \\ \Delta_{j-1} - 2\pi & \text{if} \phi_s^{(j)} - \phi_s^{(j-1)} > \pi \\ \Delta_{j-1} & \text{otherwise} \end{cases} \quad \text{(A5)}$$

and $\Delta_1 = 0$. (For example, the case might arise that on one grid point a phase of 2π - ε exists and on the next grid point a phase of 2π + ε′. If the angles were restricted to [0, 2π], then the latter phase would have been recorded as ε′, leading to the appearance of a jump in value of approximately 2π. Such jumps would invalidate the following analysis). Using the conditioned data, the average distance walked, d, between two data points separated by k (i.e., the average of the absolute value of the change in φ between two line scans) is compiled:

$$d(k) = \frac{1}{n_k}\sum_m \left|\phi_{m+k}^{(y)}(s) - \phi_m^{(y)}(s)\right| \quad \text{(A6)}$$

where the summation is performed over all available pairs of points in $\left\{\phi_m^{(y)}(s), m = 1, \ldots, n_y\right\}$, with number $n_k = n_y - k - 1$. If the phases are indeed governed by a random walk, then the expectation value of $d(k)$ is given by [13]

$$\langle d(k)\rangle = \delta\phi \cdot ff(k) \quad \text{(A7)}$$

where

$$ff(k) = \begin{cases} \frac{(k-1)!!}{(k-2)!!} & n \text{ even} \\ \frac{k!!}{(k-1)!!} & n \text{ odd} \end{cases} \quad \text{(A8)}$$

with X!! indicating the double factorial $X(X–2)(X–4)\ldots1$ with 0!! = 1. The step size of the random walk is therefore calibrated from the data by fitting the experimental values for $d(k)$ according to

$$\delta\phi = \frac{\sum_k w_k \frac{d(k)}{ff(k)}}{\sum_k w_k} \quad \text{(A9)}$$

where the weight factors $w_k = n_y - k - 1$. Finally, the deduced value δφ is normalized by the distance δy between line scans on the experimental specimen to yield the characteristic length:

$$\kappa_\phi^{(y)}(s) = 1 \Big/ \frac{\delta\phi}{\delta y} \quad \text{(A10)}$$

Formulae for the Fourier decomposition of the warp packing density $\delta_{yy}^S(x, y)$ in the y-direction can be obtained from the preceding analysis by permuting x and y in all subscripts and superscripts. The resulting complex Fourier coefficients have amplitudes $A_m^{(x)}(s)$ possessing mean $M_A^{(x)}(s)$, standard deviation $\sigma_A^{(x)}(s)$, and correlation length $\kappa_A^{(x)}(s)$; and phase angles $\phi_m^{(x)}(s)$ possessing characteristic length $\kappa_\phi^{(x)}(s)$.

3 Reconstruction Algorithm—Generating Virtual Specimens

Virtual replicas of the experimentally measured stochastic textile are generated by the Monte Carlo method[14] using the statistical information summarized in the variables of Eqn. (3). To generate positional variations for any genus of tows, the reconstruction algorithm generates instantiations of the amplitudes and phases of the Fourier components for a sequence of scan lines normal to the tow direction. This is done by progressing from one member of the sequence of scan lines to the next, using a Markov Chain algorithm developed in[3] to generate amplitude values and the random walk model described in Section A.2 to generate phase values. The Markov Chain is governed by a Probability Transition Matrix (PTM), which is calibrated separately for each Fourier component s using the prescribed values of the mean and standard deviation, for example, $M_A^{(y)}(s)$ and $\sigma_A^{(y)}(s)$ for weft deviations, as described in.[3] The random walk is governed by Eqn. (A3). The process of generating amplitude values for the sequence of scan lines is initiated at the first scan line by choosing a value for the amplitude that is weighted by a normal distribution function with mean and standard deviation, for example, $M_A^{(y)}(s)$ and $\sigma_A^{(y)}(s)$. The process of generating phase angles is initiated by choosing a phase value for the first scan line that is weighted by a uniform distribution over [0, 2π].

When the amplitudes and phases have been generated for all Fourier components, the variations of δ_{xx}, etc., along the scan lines is found by an inverse DFT. Given these spatial derivatives, the positional deviations of the tows are found by integrating over the specimen from a chosen origin.

The positional deviations describe only the deviations of tows where they appear on the outer surfaces of the specimen. However, for thin specimens typical of textile ceramic matrix composites,[1] this information, when used in conjunction with the reconstruction algorithm for unit-cell scale deviations described in[3] and,[4] should suffice to generate

positional deviations for the entire 3D fabric. This problem will be taken up elsewhere.

Acknowledgments

This work was supported by the US AFOSR (Ali Sayir) and NASA (Anthony Calomino) under the National Hypersonics Science Center for Materials and Structures (AFOSR Prime Contract No. FA9550-09-1-0477 to Teledyne Scientific and Sub-contract No. B9U538772 to UCSB).

Supporting Information

Additional Supporting Information may be found in the online version of this article:

Fig. S1. Quasi-continuous plots of short-range spatial derivatives of the deviation data $(u_i,v_i)_s$ from the back side of the panel.

Table S1. Statistics of Amplitudes and Phases of each Spectral Mode in DFT Analysis

References

[1]D. B. Marshall and B. N. Cox, "Integral Textile Ceramic Structures," *Annu. Rev. Mater. Res.*, **38**, 425–43 (2008).

[2]H. Bale, M. Blacklock, M. R. Begley, D. B. Marshall, B. N. Cox, and R. O. Richie, "Characterizing Three-Dimensional Textile Ceramic Composites Using Synchrotron x-ray Micro-Computed-Tomography," *J. Am. Ceram. Soc.*, **95** [1] 392–402 (2012).

[3]M. Blacklock, H. Bale, M. R. Begley, and B. N. Cox, "Generating Virtual Textile Composite Specimens Using Statistical Data From Micro-Computed Tomography: 1d tow Representations for the Binary Model," *J. Mech. Phys. Solids*, **60** [6] 451–70 (2012).

[4]R. G. Rinaldi, M. Blacklock, H. Bale, M. R. Begley, and B. N. Cox, "Generating Virtual Textile Composite Specimens Using Statistical Data From Micro-Computed Tomography: 3d tow Representations," *J. Mech. Phys. Solids*, **60** [8] 1561–81 (2012).

[5]J. G. Campbell and F. Murtagh, "Automatic Visual Inspection of Woven Textiles Using a tow-Stage Defet Detector," *Opt. Eng.*, **37** [9] 2536–42 (1998).

[6]C. Chan and G. K. H. Pang, "Fabric Defect Detection by Fourier Analysis," *Ind. Appl. IEEE Trans.*, **36** [5] 1267–76 (2000).

[7]W. J. Jasper and H. Potlapalli, "Image Analysis of Mispicks in Woven Fabric," *Text. Res. J.*, **65** [11] 683–92 (1995).

[8]K. L. Mak, P. Peng, and K. F. C. Yiu, "Fabric Defect Detection Using Morphological Filters," *Image Vis. Comput.*, **27** [10] 1585–92 (2009).

[9]A. Vanaerschot, B. N. Cox, S. V. Lomov, and D. Vandepitte, Stochastic Characterisation of the in-Plane tow Centroid in Textile Composites to Quantify the Multi-Scale Variation in Geometry. International Union of Theoretical and Applied Mechanics, 2014.

[10]M. D. Novak and F. W. Zok, "High-Temperature Materials Testing With Full-Field Strain Measurement: Experimental Design and Practice," *Rev. Sci. Instrum.*, **82** [11] 115101 (2011).

[11]V. P. Rajan, M. N. Rossol, and F. W. Zok, "Optimization of Digital Image Correlation for High-Resolution Strain Mapping of Ceramic Composites," *Exp. Mech.*, **52** [9] 1407–21 (2012).

[12]M. N. Rossol, J. H. Shaw, H. Bale, R. O. Ritchie, D. B. Marshall, and F. W. Zok, "Characterizing Weave Geometry in Textile Ceramic Composites Using Digital Image Correlation," *J. Am. Ceram. Soc.*, **96** [8] 2362–5 (2013).

[13]Wolfram Research. http://mathworld.wolfram.com/RandomWalk1-Dimensional.html. 2013.

[14]N. Metropolis and S. Ulam, "The Monte Carlo Method," *J. Am. Stat. Assoc.*, **44** [247] 335–41 (1949). □